Cryogenic tritium-hydrogen-deuterium and deuterium-tritium layer implosions with high density carbon ablators in near-vacuum hohlraums

N. B. Meezan, L. F. Berzak Hopkins, S. Le Pape, L. Divol, A. J. MacKinnon, T. Döppner, D. D. Ho, O. S. Jones, S. F. Khan, T. Ma, J. L. Milovich, A. E. Pak, J. S. Ross, C. A. Thomas, L. R. Benedetti, D. K. Bradley, P. M. Celliers, D. S. Clark, J. E. Field, S. W. Haan, N. Izumi, G. A. Kyrala, J. D. Moody, P. K. Patel, J. E. Ralph, J. R. Rygg, S. M. Sepke, B. K. Spears, R. Tommasini, R. P. J. Town, J. Biener, R. M. Bionta, E. J. Bond, J. A. Caggiano, M. J. Eckart, M. Gatu Johnson, G. P. Grim, A. V. Hamza, E. P. Hartouni, R. Hatarik, D. E. Hoover, J. D. Kilkenny, B. J. Kozioziemski, J. J. Kroll, J. M. McNaney, A. Nikroo, D. B. Sayre, M. Stadermann, C. Wild, B. E. Yoxall, O. L. Landen, W. W. Hsing, and M. J. Edwards

Citation: Physics of Plasmas (1994-present) **22**, 062703 (2015); doi: 10.1063/1.4921947
View online: http://dx.doi.org/10.1063/1.4921947
View Table of Contents: http://scitation.aip.org/content/aip/journal/pop/22/6?ver=pdfcov
Published by the AIP Publishing

Cryogenic tritium-hydrogen-deuterium and deuterium-tritium layer implosions with high density carbon ablators in near-vacuum hohlraums

N. B. Meezan,[1,a)] L. F. Berzak Hopkins,[1] S. Le Pape,[1] L. Divol,[1] A. J. MacKinnon,[1] T. Döppner,[1] D. D. Ho,[1] O. S. Jones,[1] S. F. Khan,[1] T. Ma,[1] J. L. Milovich,[1] A. E. Pak,[1] J. S. Ross,[1] C. A. Thomas,[1] L. R. Benedetti,[1] D. K. Bradley,[1] P. M. Celliers,[1] D. S. Clark,[1] J. E. Field,[1] S. W. Haan,[1] N. Izumi,[1] G. A. Kyrala,[2] J. D. Moody,[1] P. K. Patel,[1] J. E. Ralph,[1] J. R. Rygg,[1] S. M. Sepke,[1] B. K. Spears,[1] R. Tommasini,[1] R. P. J. Town,[1] J. Biener,[1] R. M. Bionta,[1] E. J. Bond,[1] J. A. Caggiano,[1] M. J. Eckart,[1] M. Gatu Johnson,[3] G. P. Grim,[1] A. V. Hamza,[1] E. P. Hartouni,[1] R. Hatarik,[1] D. E. Hoover,[4] J. D. Kilkenny,[4] B. J. Kozioziemski,[1] J. J. Kroll,[1] J. M. McNaney,[4] A. Nikroo,[4] D. B. Sayre,[1] M. Stadermann,[1] C. Wild,[5] B. E. Yoxall,[1] O. L. Landen,[1] W. W. Hsing,[1] and M. J. Edwards[1]
[1]*Lawrence Livermore National Laboratory, P.O. Box 808, Livermore, California 94551-0808, USA*
[2]*Los Alamos National Laboratory, P.O. Box 1663, Los Alamos, New Mexico 87545, USA*
[3]*Massachusetts Institute of Technology, 77 Massachusetts Avenue, NW16, Cambridge, Massachusetts 02139, USA*
[4]*General Atomics, P.O. Box 85608, San Diego, California 93286-5608, USA*
[5]*Diamond Materials GMBH, Hans-Bunte-Str. 19, 79108 Freiburg, Germany*

(Received 14 February 2015; accepted 18 May 2015; published online 2 June 2015)

High Density Carbon (or diamond) is a promising ablator material for use in near-vacuum hohlraums, as its high density allows for ignition designs with laser pulse durations of <10 ns. A series of Inertial Confinement Fusion (ICF) experiments in 2013 on the National Ignition Facility [Moses *et al.*, Phys. Plasmas **16**, 041006 (2009)] culminated in a deuterium-tritium (DT) layered implosion driven by a 6.8 ns, 2-shock laser pulse. This paper describes these experiments and comparisons with ICF design code simulations. Backlit radiography of a tritium-hydrogen-deuterium (THD) layered capsule demonstrated an ablator implosion velocity of 385 km/s with a slightly oblate hot spot shape. Other diagnostics suggested an asymmetric compressed fuel layer. A streak camera-based hot spot self-emission diagnostic (SPIDER) showed a double-peaked history of the capsule self-emission. Simulations suggest that this is a signature of low quality hot spot formation. Changes to the laser pulse and pointing for a subsequent DT implosion resulted in a higher temperature, prolate hot spot and a thermonuclear yield of 1.8×10^{15} neutrons, 40% of the 1D simulated yield. © *2015 AIP Publishing LLC*. [http://dx.doi.org/10.1063/1.4921947]

I. INTRODUCTION

In the inertial confinement fusion (ICF) hot spot ignition scheme, kinetic energy from an imploding spherical pusher is converted upon stagnation to internal energy in the fusion fuel hot spot.[1] The fusion capsule consists of a thin shell of cryogenic deuterium-tritium (DT) fuel surrounded by a low-Z ablator. For most experiments at the National Ignition Facility (NIF),[2] the capsule is imploded with the indirect-drive method. Laser power deposited inside a gold or uranium hohlraum is converted to soft x-rays that impinge on the ablator. The ablator material absorbs the x-rays and explodes outward, accelerating the shell inward. Achieving a sufficiently high hot spot temperature to initiate thermonuclear (TN) burn requires a maximum velocity of the cryogenic DT fuel pusher of $V_{fuel} = 350$ km/s or greater.[3] Nearly all ICF experiments on the NIF to date have used a plastic (CH) ablator; however, high-density carbon (HDC), or diamond, and beryllium ablators have recently been used for implosions on the NIF.[4]

HDC is under study because its material properties are different from CH. HDC has a density of $\rho \gtrsim 3.3$–3.5 g/cm^3, compared to $\rho \approx 1$ g/cm^3 for CH. The density difference manifests itself most clearly in the multi-step laser pulses required to drive a high compression ICF implosion. Ignition pulses can be 8–10 ns in duration for an HDC ablator, compared with 15–22 ns in duration for a CH ablator of similar mass. This opens the possibility of driving ignition relevant implosions with HDC ablators in near-vacuum hohlraums. While most indirectly driven ICF experiments on the NOVA and OMEGA laser facilities have used vacuum hohlraums, experiments on the NIF have primarily used helium-filled hohlraums with initial gas densities of $\rho \gtrsim 1$ mg/cm^3. The gas fill serves to tamp the expansion of the hohlraum wall and is necessary to prevent the hohlraum from filling with gold during long-duration laser pulses. In contrast, a near-vacuum hohlraum has a very low density gas fill, $\rho = 0.03$–0.06 mg/cm^3. This amount of gas fill is sufficient to provide a conduction path between the capsule and the hohlraum wall for cryogenic layering but is not expected to tamp the hohlraum wall expansion during the experiment.

This paper describes a set of four experiments that demonstrated that the HDC ablator in a near-vacuum hohlraum is a viable candidate for achieving alpha heating and ignition on the NIF. In addition, this experimental campaign serves as an example of how radiation hydrodynamic design codes

a)Electronic mail: meezan1@llnl.gov

such as HYDRA[5] can be used to understand and improve upon ICF experiments, even with incomplete physical models and imperfect predictive capability. In this case, a working model with physically motivated *ad hoc* adjustments was constructed to improve agreement with basic implosion timing and with primary x-ray imaging diagnostics. It was found that for the third experiment of the campaign, the first HDC ablator experiment with a cryogenic fuel layer, this model also showed excellent agreement with secondary diagnostics, such as x-ray burn history. This increased confidence in the model's accuracy and utility. The model provided insight into the implosion dynamics and guided improvements for a subsequent cryogenic layered experiment. The follow-on experiment demonstrated improved thermonuclear performance while maintaining excellent agreement between the model and diagnostic data.

II. EXPERIMENTAL SETUP

A. Two-shock design in near-vacuum hohlraums

The experiments described here were conducted in near-vacuum hohlraums using a high-adiabat, 2-shock laser pulse. This design is an extension of the CH Indirect Drive Exploding Pusher[6] to higher convergence ratio. The pulse is designed to launch two shocks sequentially into the DT fuel layer, leading to an in-flight adiabat $\alpha = 3.5$. Here, the adiabat[3] is defined as $\alpha = P/P_{cold}$, where P_{cold} is the minimum pressure of DT at a density of $\rho = 1000\,\mathrm{g/cm^3}$. The value $\alpha = 3.5$ is calculated from the mass-average entropy of the fuel layer at the time of peak implosion velocity. The minimum adiabat of the cold DT fuel is $\alpha = 2.9$ by the definition above or $\alpha = 2.3$ using the more common definition[7]

$$\alpha = P/P_{Fermi} = \frac{P}{2.17\rho^{5/3}},$$

where P is megabars and ρ is in g/cm^3. This type of low compression design can achieve substantial self-heating of the hot spot by alpha particle deposition but cannot reach ignition in NIF scale targets.

Schematics of the hohlraum and capsule are shown in Fig. 1. The gold hohlraum is 5.75 mm in diameter and 10.125 mm long with a laser entrance hole (LEH) diameter

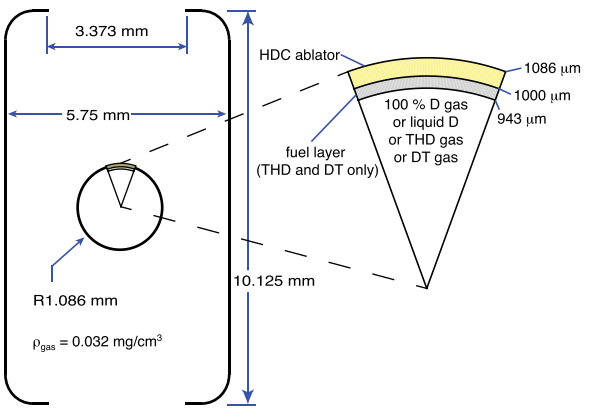

FIG. 1. Hohlraum schematic and capsule pie-diagram for 2-shock HDC ablator experiments in near-vacuum hohlraums.

of 3.373 mm. This hohlraum is a slightly longer version of the standard hohlraum used for ICF experiments on the NIF[8] and was originally tested during a length-scaling experiment with a CH capsule and a 20 ns long, 4-shock ignition laser pulse.[9] In this case, the hohlraum is filled with $\rho = 0.032\,\mathrm{mg/cm^3}$ helium gas. The hohlraum LEH's is covered with 500 nm-thick polyimide windows.

The capsules are 86 μm shells of undoped high-density carbon with 1 mm inner radius. The HDC targets used in the present study were prepared by using the plasma-assisted chemical vapor deposition (CVD) process reported by Biener.[10] Due to small amounts of hydrogen (up to 3.5 at. %) and graphitic carbon (<5%) associated with grain boundaries, nanocrystalline HDC has a lower density than coarse grained polycrystalline CVD diamond or single crystalline diamond (3.32 g/cm^3 versus 3.52 g/cm^3).[11] The capsules are filled via a 10 μm diameter glass fill tube. The cryogenic fuel layers for the experiments described here were ≈57 μm thick.

B. Target details

Experiments were performed on four target types. The first three of these experiments were described in a previous paper by MacKinnon and co-authors.[4] The experimental series culminated in a cryogenic DT implosion with the standard 50% D/50% T fuel mixture. The two cryogenic layered implosions will be described here in greater detail.

The shock-timing "keyhole" target uses a reentrant cone-in-shell geometry to provide access to the inner ablator surface. The velocity and timing of the shocks launched into the capsule are measured in liquid deuterium using a Velocity Interferometer for Any Reflector (VISAR) diagnostic.[12] The symmetry capsule or "symcap" is a gas-filled surrogate capsule with no cryogenic fuel layer used to measure the implosion symmetry and the time of stagnation or "bang time." The shape of the x-ray self-emission from the imploded core is imaged using x-ray framing cameras. In a symcap, the cryogenic fuel layer is typically replaced with additional ablator material of the same mass.[13,14] For the HDC capsules, this would be a very small thickness

$$d_{HDC} \approx \frac{\rho_{DT}}{\rho_{HDC}} d_{DT} = \frac{0.25}{3.32} 57\,\mu\mathrm{m} = 4\,\mu\mathrm{m}.$$

For the experiments described here, the symcap and cryogenic layered targets used the same thickness ablator, so the symcap was a thinner/lower-mass surrogate of the cryogenic layered implosions.

The backlit radiography target uses a backlighter foil and an x-ray framing camera to measure the shape and velocity of the ablator up to peak implosion velocity.[9] This target had a cryogenic fuel layer with a deuterium-poor "THD" mixture of 75% T, 23% H, and 2% D. This dudded THD fuel mixture enables experiments with in-flight hydrodynamics nearly identical to those of the high-yield DT implosion without the neutron and gamma-ray background.[15] The backlit radiography target configuration introduces 3D asymmetries into the implosion. Two NIF quads at azimuthal angle

of $\phi \approx 270^\circ$ are diverted from the hohlraum to an external large-area backlighter foil (nickel for this experiment). Two 800 μm × 800 μm windows cut into the hohlraum wall provide access for the backlighter x-rays and a gated x-ray detector. The combination of the missing laser quads (which leave dim spots on the hohlraum wall at $\phi \approx 90^\circ$) and the imaging windows, which occur at $\phi = 78^\circ$ and $\phi = 258^\circ$, generates large $m = 1$ and $m = 2$ azimuthal asymmetries in the implosion, making the backlit radiography experiment a poor surrogate to the cryogenic DT implosion for 3D symmetry.

For the cryogenic DT layered experiment, the only significant perturbation to the target environment is a diagnostic window to allow equatorial imaging of the capsule self emission. This window is much smaller than those used for backlit radiography. The inner surface of the window is coated with a 2.5 μm layer of gold to minimize the local perturbation to the x-ray albedo and the subsequent impact on 3D symmetry. This experiment used the standard set of x-ray and nuclear diagnostics for cryogenic implosions as described in the paper by Edwards.[15]

C. Laser pulses

The laser pulses for the four experiments are shown in Fig. 2. The symcap (N130813) and the backlit THD (N130920) used a 420 TW peak power pulse. For the symcap, one NIF quad was dropped from the experiment due to technical problems, reducing the total energy on the shot from the requested 1.35 MJ to 1.29 MJ. Based on the results of the symcap, the laser pulse duration was reduced by 200 ps for the THD, reducing the requested laser energy to 1.27 MJ. This was done to increase the amount of unablated mass surrounding the fuel layer. Simulations suggested that very little ablator would remain around the fuel at the time of peak velocity.

The keyhole experiment NIF shot N130916 used a lower power, shorter laser pulse (250 TW, 760 kJ) to prevent blanking of the VISAR diagnostic window from gold "M-band" x-rays with energy $h\nu > 1.8$ keV. The main goal of this experiment was to measure the velocity of the first shock and the merger time of the first and second shocks; these parameters are insensitive to the peak power in the main laser pulse. For the DT shot N131212, the peak laser power was reduced to 300 TW, and the pulse duration was increased by 425 ps relative to the symcap (625 ps relative to the THD), resulting in a requested energy of 1.2 MJ. The motivation behind these changes will be explained in Sec. IV D.

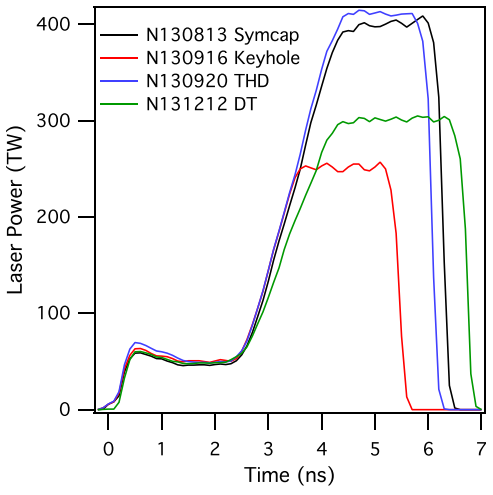

FIG. 2. Measured total laser power delivered to the hohlraum for 2-shock HDC ablator experiments in near-vacuum hohlraums.

III. RADIATION HYDRODYNAMIC MODELING

A. Baseline model

The experiments described in the paper were simulated in 2D axisymmetric geometry using the ICF design code HYDRA. HYDRA is a massively parallel, block structured mesh-based multiphysics radiation hydrodynamics code and is currently the standard design tool for NIF ICF targets.[5] HYDRA includes models for fluid flow, separate electron and ion conduction, radiation (photon) transport, laser deposition, and TN burn, including transport of the neutrons, light ions, and gamma rays generated by TN burn. The TN burn model samples the product particles produced by fusion reactions and transports them through the mesh using Monte Carlo methods and solving the full transport equation. Relativistic effects resulting from the motion of the particles and Doppler shifts resulting from flowing of the background fluid are included, as are nuclear and Coulomb collisions. A wide array of information about the particles both as they traverse the mesh and as they escape may be tallied and used to synthesize experimental observables, including neutron output spectra.

The 2D integrated (hohlraum + capsule) post-shot simulations described here use the "high-flux" hohlraum physics model developed after the NIF hohlraum energetics campaign of 2009: electron thermal conduction with a flux-limiter $f = 0.15$ and the detailed configuration accounting (DCA) non-LTE atomic physics model.[16] The post-shot simulations described in this paper use NIF target metrology and laser performance data as input conditions for HYDRA.

B. Pre-shot vs. post-shot calculations

At this point, a brief comparison of "pre-shot" and "post-shot" calculations is instructive. Pre-shot calculations are made while designing an experiment for the purposes of determining if the experiment will meet its scientific goals and for providing appropriate diagnostic settings. Pre-shot calculations use the requested laser pulses and ideal target dimensions as inputs. In the case of this paper, the pre-shot calculations were made with the baseline model described above in Sec. III A. Changes to the experiments over the course of the campaign were made based on these calculations.

The purpose of post-shot calculations is to develop a model of the implosion that agrees with as many of the experimental observables as possible. This maximizes the model's value for determining the physical processes occurring behind the observables that the model captures and helps isolate the physics driving observables that the model does not reproduce. The post-shot calculations described here differ

from pre-shots in two ways: post-shot calculations use our best measurements of the input laser pulse and target geometry–the most correct inputs for the simulations. In addition, the post-shot calculations used HYDRA with the adjustments described below in Sec. III C. The post-shot calculations have lower fuel velocity and later bang-times than the pre-shot calculations. Post-shot calculations also result in less oblate implosions. The predicted thermonuclear yields are slightly lower than the pre-shot yields.

C. Model adjustments

For hohlraums filled with high density helium gas with density of $\rho \gtrsim 1\,\mathrm{mg/cm^3}$, the laser source must be further degraded by 22%–28% (in addition to backscatter losses) to match experimental shock-front and ablator data;[17] however, for the near-vacuum hohlraums described here, very little adjustment is needed to match experimental data.[4,6,18] This makes sense: during its development, the high-flux model was bench-marked against vacuum hohlraum experiments performed on the NOVA and OMEGA laser facilities. The first demonstration of the high-flux model's utility for designing NIF experiments was its ability to reproduce x-ray intensity data from vacuum hohlraums, as reported by Olson.[19] The high efficiency of near-vacuum hohlraums for driving implosions is described in more detail in a recent paper by Hopkins.[18] The x-ray conversion efficiency $\eta_{CE} \approx 90\%$ for near-vacuum hohlraums on the NIF. For a given amount of laser energy, a near-vacuum hohlraum can drive a capsule with 30%–40% more x-ray intensity than one filled with helium gas of $\rho \gtrsim 1\,\mathrm{mg/cm^3}$.

The simulations of the THD experiment N130920 and the DT experiment N131212 were adjusted in two ways to match experimental measurements. The laser power and energy in the main (second) pulse were reduced by 10% to bring the simulated time of capsule peak x-ray emission bang time into agreement with data. A power reduction of 10% corresponds to a delay of $\Delta t \approx 200$ ps in bang time. Note that the start time of the laser pulse relative to the bang time is known to ≈30 ps, and the laser power and energy delivered to the hohlraum are measured with an uncertainty of ≈2%. The overall systematic error of bang time measurements on NIF is ≈60 ps. The 10% *ad-hoc* reduction in laser power likely compensates for a slight over-estimation of the emissivity of gold plasma by the high-flux model in HYDRA; however, it could also be due to uncertainty in the x-ray opacity of carbon. For the experiments described here, laser backscatter and hot electron generation were too small to be significant[18] and were not included in post-shot simulations.

The second adjustment relates to implosion symmetry. Recent experiments on the NIF in near-vacuum hohlraums have typically resulted in more prolate ("sausage") implosions than predicted by HYDRA.[20] The basic physics of symmetry control for vacuum hohlraums is essentially the same as for more conventional gas-filled hohlraums. The NIF laser beams are grouped into an inner cone with polar angles of 23.5° and 30° relative to the hohlraum axis and an outer cone with polar angles of 44.5° and 50° relative to the hohlraum axis. The polar radiation flux asymmetry seen by the capsule can be expressed in a Legendre polynomial decomposition with polynomial order l. The $l = 4$ flux P_4 is controlled by locating the beam spots on the walls such that the inner cone and outer cone contributions to the P_4 flux cancel out. The $l = 2$ flux P_2 is controlled by adjusting the brightness of the inner cone beams relative to the outer cone beams. For a spherical capsule inside a cylindrical hohlraum, this requires the x-ray spots to have an inner:outer balance of approximately 1:4. In gas-filled hohlraums with density of $\rho \gtrsim 1\,\mathrm{mg/cm^3}$, the inner cone laser beams are attenuated by the inverse bremsstrahlung in the gas plasma, so achieving the x-ray brightness ratio of 1:4 at the hohlraum wall requires a laser power balance of nearly 1:1 inner:outer. Inner cone laser propagation is further impaired by the Stimulated Raman Backscatter (SRS) instability.[21] In practice, symmetry control in gas-filled hohlraums is achieved by adjusting the wavelengths of the beams to control the level of cross-beam energy transfer (CBET): the amount of power transferred to the inner cone is increased until absorption and SRS are overcome.[22,23]

Laser propagation in vacuum hohlraums behaves differently. Initially, there is very little plasma in the path of the laser beams, so the inner cone beams propagate freely to the hohlraum wall equator. In addition, the plasma in the LEH region where the inner and outer cone beams overlap has very low density and high electron temperature compared with conventional gas-filled hohlraums. Calculations of CBET using these plasma conditions show very small levels of transfer between inner and outer cone laser beams, ≪10%. Thus, implosion symmetry can be controlled by adjusting the laser powers directly–for example, see Fig. 3. This method, called dynamic beam phasing, is described in more detail in a paper by Berzak Hopkins.[20] The inner-cone fraction for the first 2.5 ns of N130920 is indeed 20%, an inner:outer balance of 1:4.

As the experiment progresses, the hohlraum begins to fill with plasma from the gold hohlraum wall and the HDC ablator. In HYDRA simulations of these implosions, the low density ablator and gold flows collide near the hohlraum waist, creating a thin ridge of plasma with density comparable to the critical density for 351 nm light. This ridge stops part of the inner cone laser beams from reaching the hohlraum wall. Since HYDRA is a single-fluid ALE code, the density of this feature and its subsequent effect on laser propagation are likely over-estimated. It has been known for some time that the interaction of ablated gold and capsule material in a vacuum hohlraum is initially collisionless,[24] as the ion-ion mean-free-paths of such flows are hundreds of microns.[20] Dealing with this transition in a physically meaningful way is an active area of research in the indirect drive ICF program.

This study required construction of a physically motivated integrated model that reproduces enough of the experimental data to provide insight into the implosion. This was accomplished by enhancing the propagation of the inner-cone laser beams to reproduce the measured implosion symmetry. In HYDRA, inner cone propagation is enhanced by increasing the laser frequency from 3ω (351 nm) to 5ω (211 nm). This reduces the levels of refraction and inverse bremsstrahlung absorption of the beams without affecting the global hohlraum energetics. This method was inspired by

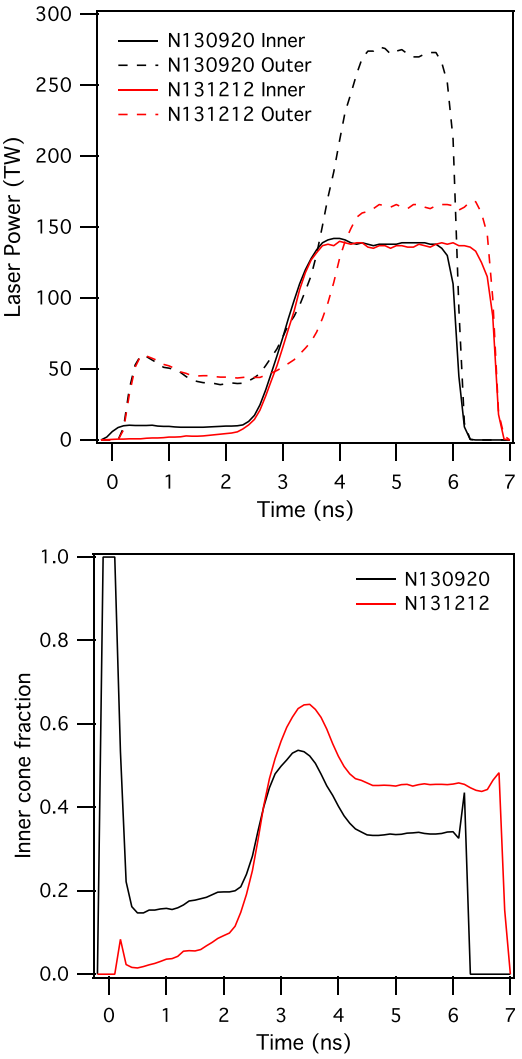

FIG. 3. Inner and outer laser pulse comparison (top) and inner cone fraction comparison (bottom) of THD experiment N130920 and DT experiment N131212.

the previous design studies of "impaired propagation," where laser light scattered by the SRS instability is reabsorbed in the hohlraum, resulting in symmetry changes but no loss of x-ray drive.[3,25] The enhanced propagation model will be compared with implosion symmetry measurements in Sec. IV. Additional comparisons of the enhanced propagation model with experiential data are shown elsewhere.[20]

IV. RESULTS AND ANALYSIS

This section describes four experiments using the laser pulse shapes shown in Fig. 2. Three of these experiments were described in the previous papers by MacKinnon and Berzak Hopkins.[4,18,20] Some details are repeated here for completeness.

A. Symcap N130813

The first implosion with an HDC ablator using the 2-shock laser pulse in a near-vacuum hohlraum was a gas-filled symmetry capsule. The primary measurement for this experiment was the x-ray self emission of the capsule. The time-integrated self-emission is shown in Fig. 4. Unfortunately, the x-ray framing camera did not trigger at the right time to capture a time-dependent record of the implosion. The image was rather large for a symcap–the average radius was 91 μm rather than the 50–60 μm typical of a plastic gas-filled NIF capsule. This corresponds to a convergence ratio of approximately 10×. The implosion is also extremely round. The asymmetry of the hot spot as expressed as a Legendre polynomial decomposition of the radius of the 17% brightness contour (the white contour line in Fig. 4) is $a_l/a_0 = 3\%$ or less for modes $l = 1$–4. The roundness of this implosion is related to its large radius, as asymmetries are amplified by convergence. In addition, the large radius is evidence of pre-heat and possible "burn-through" of the ablator by the hohlraum x-ray drive. HYDRA simulations for which the drive was adjusted to match the measured bang time also showed a large hot spot (≈100 μm) due to the x-ray ablation wave completely penetrating the HDC ablator. Calculations of this drive for a similar capsule with a DT fuel layer predict a fuel velocity of $v_{fuel} = 415$ km/s.

B. Keyhole N130916

The NIF shot N130916 was the first test of shock-timing in a near-vacuum hohlraum on NIF. This experiment was designed to measure the break-out time of the first shock from the HDC ablator into a column of liquid deuterium, the velocity of the first shock in the deuterium, the overtake time of the first shock by the second (main) shock, and the velocity of the combined shock. The location of the shock merge is assessed by integrating the velocity history. The interpreted velocity data are shown in Fig. 5, along with shock velocities interrogated from a 2D integrated HYDRA simulation (dashed). Note that the shock velocities extracted from HYDRA are not a physically complete prediction of the VISAR signal–for example, changes in refractive index are not considered; however, this comparison is good enough to determine if the simulations are providing a reasonable representation of the experiment.

The data show several notable features. In contrast with transparent ablators such as CH (plastic) or single-crystal

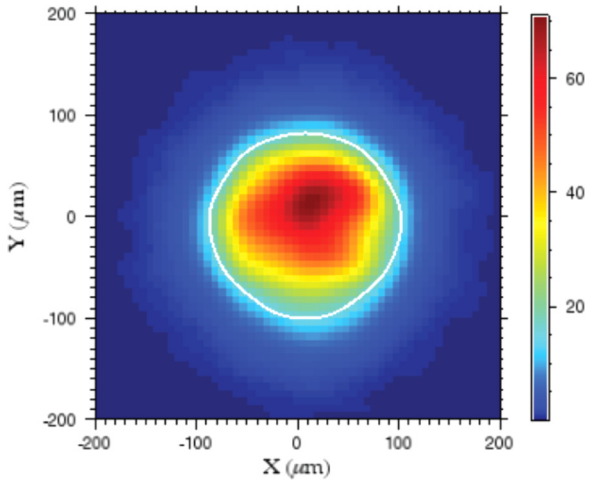

FIG. 4. Time-integrated equatorial x-ray self emission image of the gas-filled symmetry capsule for NIF shot N130813.

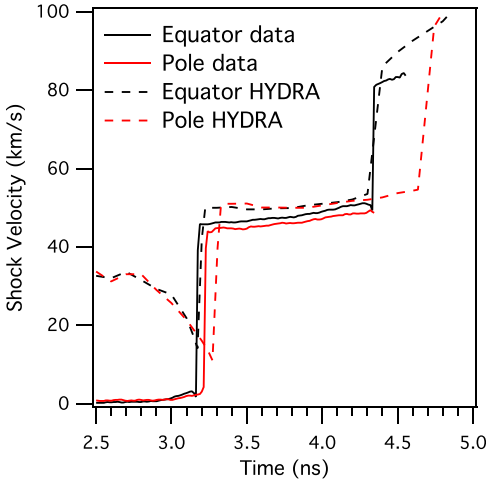

FIG. 5. Polar and equatorial shock velocity measurements from NIF shot N130916, compared with shock velocities extracted from a HYDRA simulation (dashed).

diamond, the shock velocity cannot be tracked in the HDC ablator. The nano-crystalline diamond structure scatters most of the incident light, making the HDC opaque to the VISAR laser. The VISAR does measure motion of the ablator/deuterium interface a few hundred picoseconds before shock break-out (between 2.9 and 3.2 ns in Fig. 5). This is likely evidence of x-ray induced preheat of the ablator. This experiment used an HDC ablator with no mid-Z or high-Z dopants, so x-rays with energies of $h\nu > 1.8$ keV can penetrate to this interface. The pre-heat induced motion occurs when the laser power increases at 3 ns (see Fig. 2) and accelerates the interface to ≈3 km/s. The break-out time of the first shock occurs at 3.17 ± 0.05 ns on the equator and 3.21 ± 0.05 ns on the pole, indicating a symmetric launch of the first shock from the hohlraum x-rays. The break-out times from the HYDRA simulation agree with the experiment to within 50 ps on the equator and 100 ps on the pole.

The asymmetry in first shock velocity is also small: the measured shock velocity on the equator is ≈3% faster than on the pole. The first shock velocity increases from ≈45 km/s to ≈51 km/s between shock break-out and the shock 1–2 merger on the equator. The first shock velocities in the HYDRA simulation are slightly higher than measured, increasing from ≈49.5 km/s to ≈53 km/s over the same time. The time of the shock 1–2 merger on the equator is also well matched by the simulation. The shock 1–2 merger is not observed on the pole, as the VISAR diagnostic went blank before this occurred. The asymmetric shock break-out between pole and equator is a consequence of the dynamic beam phasing approach to symmetry control–this feature of the design will be discussed further in Sec. IV D.

C. THD with back-lit radiography N130920

The good agreement between data and simulations (Fig. 5) demonstrated that a THD or DT experiment with a cryogenic layer would be adequately shock-timed. The back-lit THD implosion N130920 was shot shortly after the keyhole N130916. This experiment is described in a previous paper by MacKinnon;[4] we elaborate further here. To avoid complete burn-through of the ablator, the laser pulse duration and energy were reduced compared with the symcap N130813 (see Fig. 2). The implosion appeared to be quite symmetric based on back-lit radiography of the ablator near the time of peak velocity. A composite transmission image[26] constructed from four individual frames is shown in Fig. 6. Legendre polynomial decomposition of the transmission minimum gives an average radius of $a_0 = 190\ \mu$m. The mode-2 asymmetry is small, $a_2 = 0 \pm 2\ \mu$m. This level of asymmetry in the incoming shell is equivalent to a hot-spot asymmetry $|a_2/a_0| < 10\,\%$.

The time-integrated x-ray self emission images from the capsule are shown in Fig. 7. The equatorial view (Fig. 7(a)) shows a slightly oblate hot spot, $a_2 = -7\ \mu$m. This is consistent with a fairly round implosion as seen in back-lit transmission images, Fig. 6; however, the polar view (Fig. 7(c)) adds a wrinkle to this analysis. The hot spot shows a pronounced oblong shape with a hint of two separate lobes of emission. The oblong spot is oriented along an axis at $\phi = 78^\circ$, between 1 and 2 o'clock on the image. This axis coincides with the 800 μm square imaging windows needed for back-lit imaging, suggesting that the radiation asymmetry introduced by the diamond windows (which have lower x-ray albedo than the surrounding gold hohlraum) has perturbed the implosion. Note that if the implosion were viewed along the equator from any other azimuth ϕ, its lateral extent would be larger and the implosion would appear more oblate. Also note that the m = 1 asymmetry from bottom-left to top-right, aligned with the dim spots on the hohlraum wall where backlighter quads have been removed. It also appears that some high density gold from the hohlraum wall is obscuring the image, making the interpretation of small-scale features in this image highly uncertain.

The time-history of the average radius a_0 of the transmission minimum shows a maximum ablator velocity $v_{abl} = 385 \pm 25$ km/s. This measurement is used to estimate the velocity of the imploding fuel[4] as $v_{fuel} = 410 \pm 25$ km/s, far higher than the typical velocity of a CH ignition design, $v_{fuel} \approx 350$–370 km/s. Thus, despite some 3D asymmetry

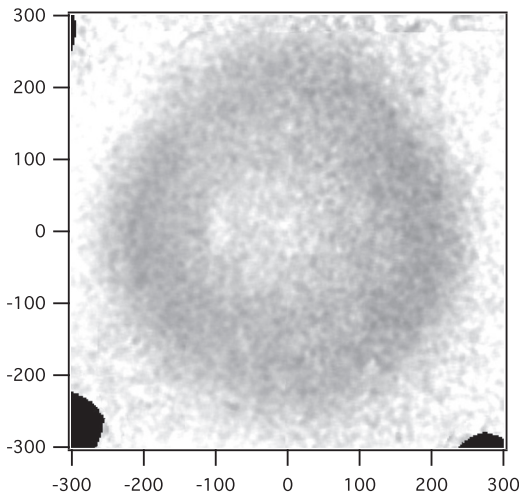

FIG. 6. Tomographic composite transmission image at ablator radius $R_{limb} = 190\ \mu$m for THD implosion N130920 back-lit by a nickel backlighter (7.8 keV). Axis units are μm.

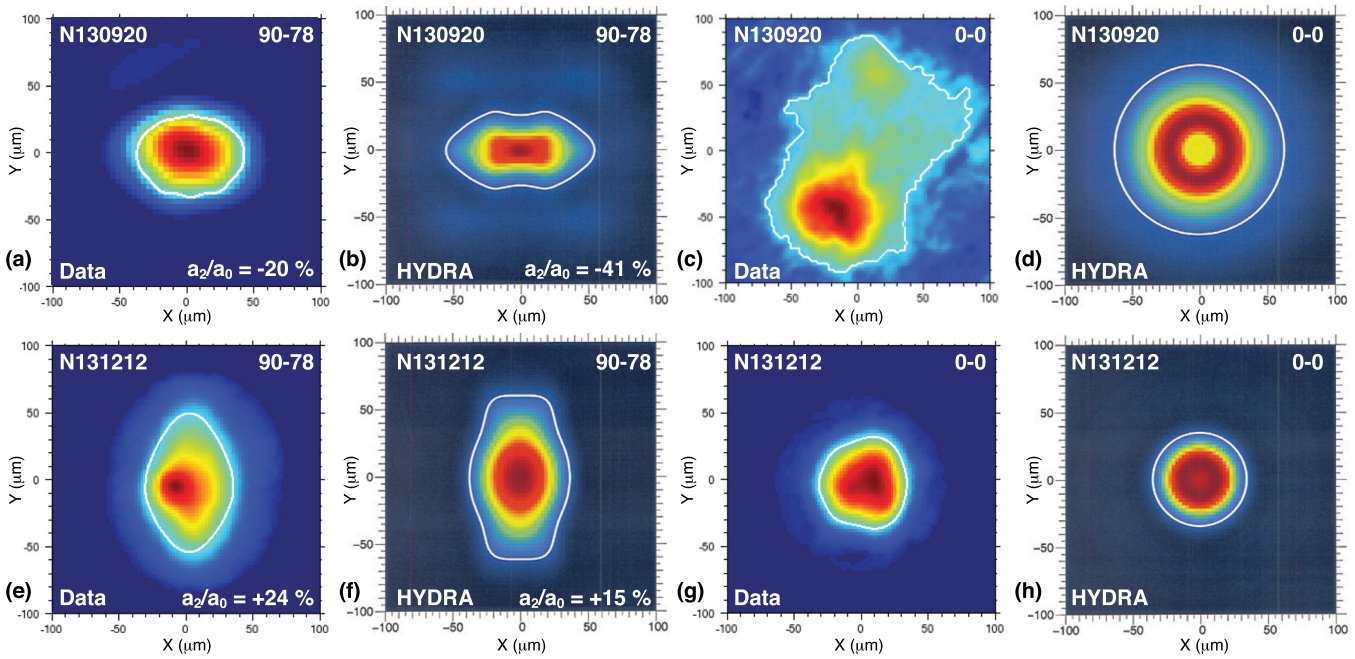

FIG. 7. Time-integrated self emission images for THD experiment N130920 and DT experiment N131212 from the equatorial (90-78) and polar (0-0) views, compared with simulated images from 2D HYDRA simulations. The HYDRA simulations use physics model adjustments described above in Sec. III.

seen in the polar x-ray image, one might expect this implosion to generate a high thermonuclear yield; however, this was not the case. A 1D simulation that matches the measured velocity and bang time produces a thermonuclear yield of $Y_n = 2.5 \times 10^{14} \pm 0.2 \times 10^{14}$. Experiment N130920 produced 2.1×10^{13} DT neutrons, or 8% of the 1D expectation.

Note that there is additional uncertainty in the expected yield due to the THD gas mixture. In THD fuel mixtures, the central gas at shot time has a different composition than the cold fuel. For N130920, the cold fuel composition was 75% T, 23% H, and 2% D; however, the equilibrium composition of the central gas at shot time was composed of ≈70% hydrogen and 1% deuterium. Therefore, the initial central gas fuel mixture is approximately 10× less reactive than the cold fuel. The hot-spot at stagnation is formed by a mixture of the initial central gas and cold fuel that has ablated. In a 1D simulation, the initial central gas remains at the center of the hot-spot and experiences the highest temperature; it is possible that processes which would normally reduce the hot-spot temperature like mix at the hot-spot/cold fuel boundary could actually increase the predicted yield.

For this experiment, the uncertainty was compounded by the fuel mixture's age of over 400 h, which resulted in more ^{3}He production than is typical for cryogenic layers on the NIF. The additional ^{3}He comprised 12% of the central gas cavity and increased its density $\rho \approx 0.4\,\mathrm{mg/cm^3}$ for "young fuel" to $\rho \approx 0.5\,\mathrm{mg/cm^3}$. The presence of the ^{3}He decreased the thermonuclear yield by 10% relative to a 1D simulation with young fuel. Nonetheless, it is clear that the nuclear performance was below expectations for this experiment and that this performance is difficult to explain using only data from x-ray imaging diagnostics. Therefore, we turn to secondary diagnostics and simulations to gain a better understanding of the implosion.

Further information on the shape of the imploded dense fuel and hot spot can be gleaned from secondary diagnostics. The neutron time-of-flight (nToF) spectrometers measure the arrival time history of fusion neutrons at several positions on the NIF target chamber.[27] The down scattered ratio (DSR) provides a measurement of the fuel ρR and is defined as

$$\mathrm{DSR} = \frac{\int_{E=10\,\mathrm{MeV}}^{E=12\,\mathrm{MeV}} f(E)dE}{\int_{E=13\,\mathrm{MeV}}^{E=15\,\mathrm{MeV}} f(E)dE},$$

where $f(E)$ is the detected neutron spectrum. Data from nToF spectrometers at different positions on the NIF target chamber provide insight into the ρR asymmetry accumulated by the dense fuel during the implosion.[15] The measured DSR versus polar angle θ is compared to 2D HYDRA simulations in Fig. 8. The simulations reported here utilize HYDRA's Particle Monte Carlo package (cf. Sec. III above) to extract neutron spectra in ten bins of equal solid angle between 0° and 90°. The data reported for this shot come from three quasi-orthogonal views, the 20 m nToF "equator" spectrometer ($\theta = 90°, \phi = 174°$), the 20 m nToF "alcove" spectrometer ($\theta = 116°, \phi = 316°$), and the 18 m nToF "south pole" spectrometer ($\theta = 161°, \phi = 56°$). The DSR varies from 1.1% to 2.8% over $\Delta\theta = 71°$, consistent with a large mode 2 polar asymmetry in the dense fuel ρR. The HYDRA simulation shows a similar, albeit much smaller, pole-high ρR variation. It is likely that there is also a 3D character to the ρR variation in the dense fuel that is not captured by the 2D HYDRA simulation.

The evolution of this ρR asymmetry at stagnation can be observed in the post-shot HYDRA simulation of N130920 (Fig. 9). The density of the imploding shell at a radius of 200 μm, near peak velocity, is shown in Fig. 9(a) (left). The

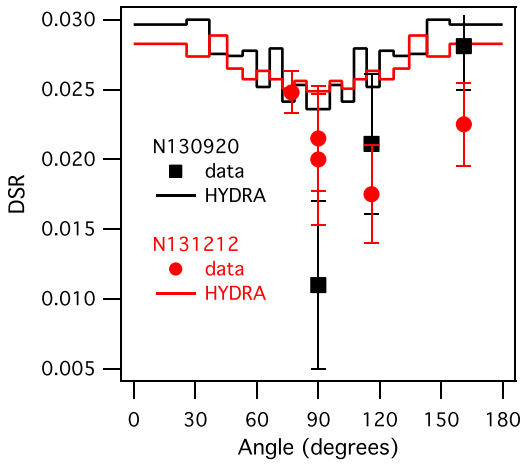

FIG. 8. Down-scattered ratio (DSR) vs. polar angle θ for THD experiment N130920 and DT experiment N131212.

shell is nearly round; however, the density of the fuel on the pole is larger than at the equator. As the shell decelerates, mass flows towards the pole. This "polar ice cap" forms an inward-facing jet that penetrates the hot spot at the onset of thermonuclear burn, as seen in Fig. 9(d) (left). Note that while the density of the pole is ≈3× the density at the equator, HYDRA predicts a DSR variation of only ≈20%. This is because the down-scattered neutrons emitted by a distributed hot spot but collected by a point detector originate from a fairly large solid angle of dense fuel. Due to the kinematics of down-scattering collisions into the $E = 10$–12 MeV range, a single nToF spectrometer samples approximately 10% of the cold fuel.[15]

The effect of the polar jets launched into the hot spot is readily visible in synthetic x-ray images from 2D HYDRA simulations (Figs. 7(b) and 7(d)) but is difficult to observe in x-ray image data (Figs. 7(a) and 7(c)) due to the 3D nature of the hot spot; however, the cooling of the hot spot by these jets can be seen indirectly in the time-history of the hot spot self-emission. The self emission history is measured with ≈23 ps resolution by the SPIDER (Streaked Polar Instrumentation for Diagnosing Energetic Radiation) filtered x-ray streak camera.[28] SPIDER typically shows a Gaussian self-emission history for NIF ICF implosions. Experiment N130920 unexpectedly presented a double-peaked self-emission history (Fig. 10). When the HYDRA simulation for N130920 was post-processed to generate a virtual SPIDER signal, this double-peaked history was very closely reproduced. This suggests that despite the 3D nature of the imploded fuel assembly, the dynamics of the stagnation and hot spot formation for experiment N130920 were well-captured by the 2D HYDRA simulation. The bang time is ≈20 ps early for the HYDRA simulation. This Δt is smaller than the SPIDER diagnostic's cross-timing accuracy relative to the NIF laser and corresponds to approximately 1% in energy coupled to the ablator. The relative height of the second peak to the first peak is well-matched by the HYDRA simulation of N130920. Closer examination of the HYDRA

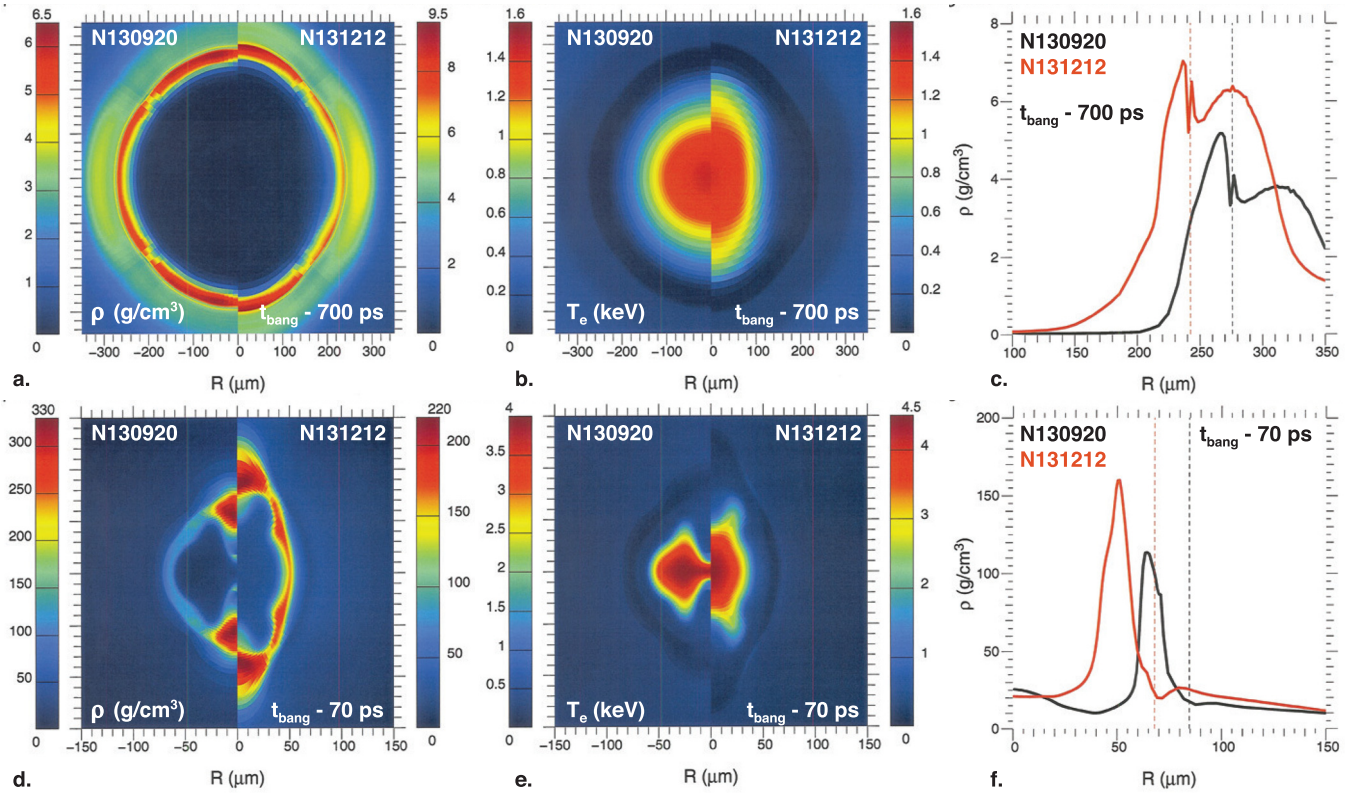

FIG. 9. Simulated density ρ (a) and electron temperature T_e (b) for experiments N130920 and N131212 are shown at time $t = t_{bang} - 700$ ps, near the time of peak v_{fuel}. The density profile along the equator is also compared (c). The dashed line shows the fuel/ablator interface. The fuel and ablator are higher density for N131212, and there is more ablator mass remaining. The simulated ρ (d) and T_e (e) are also shown at time $t = t_{bang} - 70$ ps, at the onset of hotspot burn. Note that the density and temperature color scales are different for the two experiments: N131212 has lower density polar ice caps than N130920 and reaches a higher central hot spot temperature. The density profile along the equator at this time (f) also shows more ablator mass remaining for N131212.

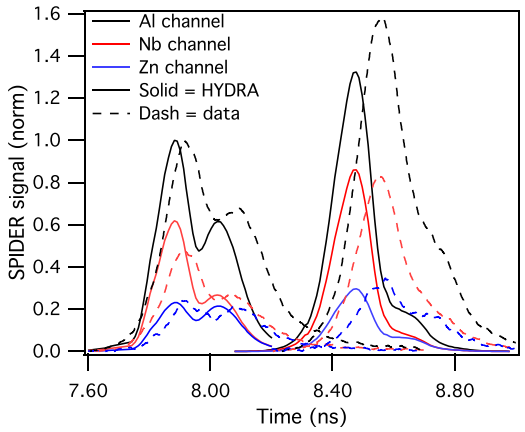

FIG. 10. Hot spot self-emission history measured by the x-ray streak camera SPIDER for experiments N130920 and N131212. Simulated SPIDER signals from post-processed HYDRA calculations are shown in solid lines.

simulation reveals the source of the second peak: the carbon ablator. The onset of capsule deceleration occurs when the return wave reflected from the hot spot origin reaches the dense fuel. At the time of stagnation, the return shock exits the dense fuel and enters the ablator, the density of which is decreasing with radius. When the shock transits and heats ablated material of low enough density, that material emits. This process is explained in more detail in a paper by Pak.[29] A radiating reflected shock has been observed after bang time in gated x-ray images of many cryogenic layered implosions with CH ablators on NIF. The ablator emission for N130920 appears different because the ablator density is much lower for this high velocity implosion using an undoped HDC ablator; thus, the radiative shock occurs earlier relative to bang time and is bright relative to the hot spot fuel emission.

Post-processed SPIDER traces from HYDRA (Fig. 11) demonstrate that the second emission peak originates entirely from the HDC ablator. The HEX post-processor for HYDRA was used to generate the synthetic x-ray images in Fig. 7 and the synthetic SPIDER traces in Figs. 10 and 11. HEX solves the radiation transport equation along straight rays traced through the simulation mesh

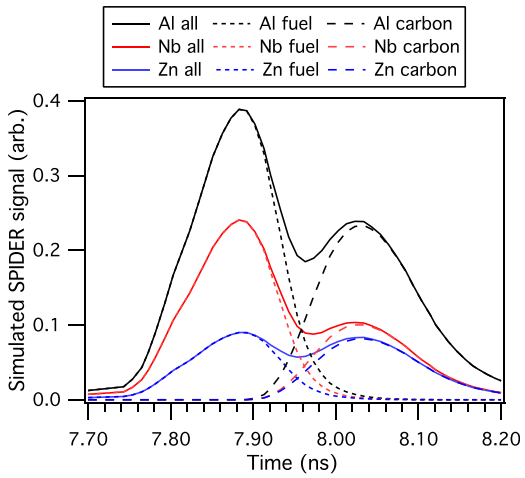

FIG. 11. Simulated SPIDER signals from post-processed HYDRA calculations of N130920. Dot: emission from THD fuel only; Dash: emission from carbon only; and Solid: total emission.

$$\frac{dI_\nu}{dz} = -\kappa_\nu I_\nu + j_\nu = -\kappa_\nu (I_\nu - \epsilon_\nu). \quad (1)$$

Here, $I(\nu) = I_\nu$ is the spectral intensity, κ is the absorption opacity in cm^{-1}, and $j_\nu = \epsilon_\nu \kappa_\nu$ is the emissivity.[30] In the short dashed curves in Fig. 11, the emission coefficient ϵ of carbon (but not the absorption coefficient κ) has been set to zero, such that only emission from THD fuel contributes to the signal. The second emission peak is entirely absent, as it originates from carbon emission.

The relative heights of the THD and carbon emission peaks are determined by two physical processes. The height of the first peak is related to the temperature and density of the fuel hot spot. The height of the second peak is related to the strength of the outgoing shock and to the density of the carbon at the fuel/ablator interface. Figure 9(f) also shows the density profile at the equator of the post-shot HYDRA simulation of N130920. The ablator has been completely penetrated by the radiation wave, leaving a large density jump between the cold fuel and the ablator.

The near-equal heights of the two peaks suggest that the implosion could be improved by increasing the remaining ablator mass and by increasing the hot spot temperature. The excellent qualitative agreement between the simulated and measured SPIDER traces increases our confidence that the HYDRA model can be used to test improvements to the implosion. These improvements are described in Sec. IV D.

D. Design changes leading to DT N131212

In order to improve the quality of the implosion and generate a less perturbed hot spot, several changes were made to the culminating cryogenic DT layer experiment N131212. Simulations indicated that it would be difficult to remove the time-dependent asymmetry that led to the angular variation in ρR observed on N130920 and the associated polar jets; however, the impact of the jets on the hot spot would be greatly reduced in a prolate implosion compared to a round or oblate ("pancake") implosion. Three changes were made to drive a prolate implosion:

(1) The total laser power and energy into the hohlraum were reduced (see Fig. 2). This also increased the ablator mass remaining.
(2) The inner cone fraction was increased from 33% to 45% during the main drive (see Fig. 3).
(3) The laser beams in the 44.5° cones were repointed closer to the capsule by 550 μm.

The motivations behind these changes are described below.

The inner and outer laser pulses for the experiments described here utilized "dynamic beam phasing" to generate a round hot spot at stagnation.[20] In this case, the inner cone laser beam power is increased faster than the outer cone power during the rise to peak power, when the laser propagates freely to the hohlraum wall. This is illustrated in Fig. 3. This results in a strong waist-hot x-ray drive on the capsule. As the hohlraum fills with gold and inner cone propagation becomes difficult, the drive swings to pole-hot. The time-average of the x-ray drive is symmetric, resulting in a round

hot spot. This approach worked for the symcap experiment N130813 (Fig. 4). Unfortunately, the large swing in P_2 drive imprints a density perturbation on the cold, dense fuel that grows into the polar ice-cap/polar jet configuration of Fig. 9.

Design simulations in HYDRA suggested that it would be difficult to maintain a near-spherical hot spot without resorting to this intentional symmetry swing, so it was left in the laser pulse for N131212. To ensure a prolate implosion that would reduce the impact of the polar jets on the hot spot, the 44.5° cone pointing was moved towards the capsule, reducing the leverage for polar P_2 flux. Note that this change required decreasing the inner-cone fraction from 20% to <10% at the beginning of the laser pulse, when the laser propagates unimpeded to the hohlraum wall (Fig. 3). In addition, the inner cone fraction during the main laser drive was increased from 33% to 45%. Since the inner cone power was already at 135 TW, near the peak of the NIF operating range, the cone fraction was increased by leaving the inner cone power constant and decreasing the outer cone power. This reduced the total power delivered from 420 TW to 300 TW. To partially compensate for the loss in fuel velocity due to the power reduction, the pulse duration was increased.

The effects of these changes in HYDRA simulations are shown in Fig. 9. At a radius of ≈200 μm, near the time of peak velocity (≈700 ps before bang time), the dense shell for N131212 is very prolate, compared to the round shell for N130920. The developing "polar ice cap" region of high fuel ρR is still evident in N131212 (Fig. 9(a) right); however, this feature has not developed into a jet at the onset of burn, 70 ps before stagnation ((Fig. 9(d) right). Despite a lower maximum fuel velocity, N131212 has a higher central electron temperature than N130920 at the onset of burn (Fig. 9(e)). The variation in DSR with angle is still quite large for N131212, varying by 0.75% out of an average of 2.3% (Fig. 8). This is less angular variation than observed in N130920. HYDRA simulations are qualitatively consistent, predicting less angular variation for N131212 than for N130920; however, the measured variation in DSR is still larger than calculated in 2D simulations–this may be due to 3D effects.

Evidence of a higher central electron temperature is seen in SPIDER measurements of hot spot self emission (Fig. 10). N131212 has a later bang time than N130920 by 600 ps, consistent with lower fuel velocity; however, the maximum x-ray intensity is 40% higher than for N130920. Despite the reduced laser energy, the maximum fuel velocity still reaches an ignition-relevant $v_{fuel} = 350$ km/s in the HYDRA simulation. In addition, the carbon emission for N131212 is slightly reduced compared to N130920, consistent with the increased ablator mass remaining outside the fuel. Overall, the change in the SPIDER signal from N130920 to N131212 is consistent with a higher quality implosion. Thermonuclear performance numbers for N130920 and N131212 are summarized in Table I. The neutron yield measured for N131212 was 1.8×10^{15}, 40% of the 1D prediction and equal to the 2D post shot simulated yield–a significant improvement in performance over N130920. Neutron yields reported here are for primary neutrons with energies of 13–15 MeV. We also provide pre-shot predictions for the two shots in Table I. The difference between pre-shot and post-shot calculations was described in Sec. III B.

TABLE I. Thermonuclear performance metrics for cryogenic layered experiments N130920 and N131212.

	N130920	N131212
Laser energy (MJ)	1.27	1.2
HYDRA v_{fuel} (km/s)	410	350
Thermonuclear yield	2.1×10^{13}	1.8×10^{15}
HYDRA 2D yield, pre-shot	8.6×10^{13}	4.7×10^{15}
HYDRA 2D yield, post-shot	6×10^{13}	1.8×10^{15}
HYDRA 1D yield, post-shot	2.5×10^{14}	5×10^{15}
Yield-over-1D (%)	3	40
Yield-over-2D (%)	31	100
Average DSR	2.36 ± 0.44%	2.3 ± 0.13%
HYDRA DSR (%)	2.69	2.65

Another important result of this experimental series is the absence of ablator mix into the hot spot. The presence of ablator material in the hot spot is inferred from x-ray emission and neutron spectral measurements. The neutron yield generated from hot DT fuel depends on the ion density, the ion temperature T_{ion}, the burn duration, and the hot spot volume. Thus, the average hot spot ion density can be calculated from the measured neutron yield, T_{ion}, burn duration, and hot spot volume (inferred from x-ray images). The x-ray emission of the hot spot depends on the same parameters, so the emission expected from a clean DT hot spot can also be calculated. Enhancement of the hot spot x-ray emission relative to clean DT is ascribed to ablator material penetrating the hot spot and radiating. Since the dependence of emission on composition through the atomic number Z is known, the x-ray enhancement can be translated into a mass of ablator material. This procedure is described in a paper by Ma.[31] Fig. 12

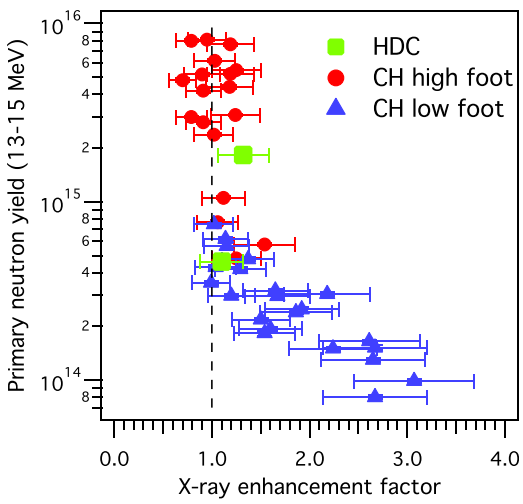

FIG. 12. DT primary neutron yield vs. x-ray enhancement factor for a subset of cryogenic DT implosions with HDC and CH ablators completed on the NIF. For shots with THD layers, the estimated equivalent DT yield is given. "Low foot" CH implosion data consist of all cryogenic layer experiments on NIF from December 2011 through March 2013. "High foot" experiments date from May 2013 through October 2014. The HDC data points are the two experiments described in this paper. For HDC, the x-ray enhancement ratio is nearly unity, similar to hydrodynamically stable "high foot" CH implosions.[31]

shows the measured neutron yield vs. x-ray enhancement for the two cryogenic layer experiments described in this paper, along with several CH ablator experiments. The x-ray enhancement levels for the HDC ablator experiments are very close to unity, suggesting that radiative cooling from ablator mixed into the hot spot is not a significant degradation mechanism for this experiment. Note that the ablator perturbation caused by the capsule fill tube is probably injecting >30 ng of ablator material. The position of a small bright spot observed on the left side of the hot spot equator in Fig. 7(e)) is consistent with a fill-tube jet.

V. CONCLUSION

A set of four experiments have demonstrated that the HDC ablator in a near-vacuum hohlraum is a viable candidate for achieving alpha heating and ignition on the NIF. This experimental campaign also showed how the design code HYDRA was used to diagnose and improve upon the first cryogenic layered experiment with an HDC ablator, N130920, despite HYDRA's lack of complete physical models for simulating the near-vacuum hohlraum. A working model constructed with an *ad hoc* enhanced laser propagation model showed good agreement with bang time and x-ray imaging diagnostics. For N130920, this model also showed excellent agreement with the x-ray burn history diagnostic SPIDER. This increased confidence in the model's utility for providing insight into the implosion dynamics and for guiding improvements for a cryogenic layered experiment with a 50%/50% D/T fuel composition. The subsequent shot N131212 demonstrated improved thermonuclear performance: neutron yield of 1.8×10^{15} and yield-over-1D of 40%, compared with $\approx$3% for N130920. The measured primary neutron yield was equal to the simulated 2D yield, suggesting that the main cause of yield degradation was the 2D prolate shape of the implosion. The working model also maintained excellent agreement with diagnostic data for N131212.

Future experiments will test different hohlraum geometries in order to drive a round implosion in a near-vacuum hohlraum with minimal symmetry swings. This will be a difficult task, as the strength of near-vacuum hohlraums (lack of laser-plasma instabilities) can also be a weakness. The cross-beam energy transfer that is ubiquitous in NIF-scale gas-filled hohlraums is a major source of uncertainty for symmetry control; however, control of $\Delta\lambda$ provides a convenient adjustment point that near-vacuum hohlraums lack. Developing an integrated design (hohlraum geometry, capsule size, and laser pulse) that enables sufficient symmetry control will likely require many experiments and calculations.

ACKNOWLEDGMENTS

The author would like to acknowledge the efforts of the NIF operations, laser performance, target diagnostics, and target fabrication teams. This work was performed under the auspices of the U.S. Department of Energy by Lawrence Livermore National Laboratory under Contract No. DE-AC52-07NA27344.

[1]J. Lindl, P. Amendt, R. Berger, S. Glendinning, S. Glenzer, S. Haan, R. Kauffman, O. Landen, and L. Suter, Phys. Plasmas **11**, 339 (2004).
[2]E. Moses, R. Boyd, B. Remington, C. Keane, and R. Al-Ayat, Phys. Plasmas **16**, 041006 (2009).
[3]S. W. Haan, J. D. Lindl, D. A. Callahan, D. S. Clark, J. D. Salmonson, B. A. Hammel, L. J. Atherton, R. C. Cook, M. J. Edwards, S. Glenzer, A. V. Hamza, S. P. Hatchett, M. C. Herrmann, D. E. Hinkel, D. D. Ho, H. Huang, O. S. Jones, J. Kline, G. Kyrala, O. L. Landen, B. J. MacGowan, M. M. Marinak, D. D. Meyerhofer, J. L. Milovich, K. A. Moreno, E. I. Moses, D. H. Munro, A. Nikroo, R. E. Olson, K. Peterson, S. M. Pollaine, J. E. Ralph, H. F. Robey, B. K. Spears, P. T. Springer, L. J. Suter, C. A. Thomas, R. P. Town, R. Vesey, S. V. Weber, H. L. Wilkens, and D. C. Wilson, Phys. Plasmas **18**, 051001 (2011).
[4]A. J. MacKinnon, N. B. Meezan, J. S. Ross, S. Le Pape, L. Berzak Hopkins, L. Divol, D. Ho, J. Milovich, A. Pak, J. Ralph, T. Döppner, P. K. Patel, C. Thomas, R. Tommasini, S. Haan, A. G. MacPhee, J. McNaney, J. Caggiano, R. Hatarik, R. Bionta, T. Ma, B. Spears, J. R. Rygg, L. R. Benedetti, R. P. J. Town, D. K. Bradley, E. L. Dewald, D. Fittinghoff, O. S. Jones, H. R. Robey, J. D. Moody, S. Khan, D. A. Callahan, A. Hamza, J. Biener, P. M. Celliers, D. G. Braun, D. J. Erskine, S. T. Prisbrey, R. J. Wallace, B. Kozioziemski, R. Dylla-Spears, J. Sater, G. Collins, E. Storm, W. Hsing, O. Landen, J. L. Atherton, J. D. Lindl, M. J. Edwards, J. A. Frenje, M. Gatu-Johnson, C. K. Li, R. Petrasso, H. Rinderknecht, M. Rosenberg, F. H. Séguin, A. Zylstra, J. P. Knauer, G. Grim, N. Guler, F. Merrill, R. Olson, G. A. Kyrala, J. D. Kilkenny, A. Nikroo, K. Moreno, D. E. Hoover, C. Wild, and E. Werner, Phys. Plasmas **21**, 056318 (2014).
[5]M. M. Marinak, G. D. Kerbel, N. A. Gentile, O. Jones, D. Munro, S. Pollaine, T. R. Dittrich, and S. W. Haan, Phys. Plasmas **8**, 2275 (2001).
[6]S. Le Pape, L. Divol, L. Berzak Hopkins, A. Mackinnon, N. B. Meezan, D. Casey, J. Frenje, H. Herrmann, J. McNaney, T. Ma, K. Widmann, A. Pak, G. Grimm, J. Knauer, R. Petrasso, A. Zylstra, H. Rinderknecht, M. Rosenberg, M. Gatu-Johnson, and J. D. Kilkenny, Phys. Rev. Lett. **112**, 225002 (2014).
[7]S. Atzeni and J. Meyer-ter Vehn, *The Physics of Inertial Fusion: Beam Plasma Interaction, Hydrodynamics, Hot Dense Matter*, International Series of Monographs on Physics (Clarendon Press, 2004), p. 52.
[8]D. A. Callahan, N. B. Meezan, S. H. Glenzer, A. J. MacKinnon, L. R. Benedetti, D. K. Bradley, J. R. Celeste, P. M. Celliers, S. N. Dixit, T. Döppner, E. G. Dzentitis, S. Glenn, S. W. Haan, C. A. Haynam, D. G. Hicks, D. E. Hinkel, O. S. Jones, O. L. Landen, R. A. London, A. G. MacPhee, P. A. Michel, J. D. Moody, J. E. Ralph, H. F. Robey, M. D. Rosen, M. B. Schneider, D. J. Strozzi, L. J. Suter, R. P. J. Town, K. Widmann, E. A. Williams, M. J. Edwards, B. J. MacGowan, J. D. Lindl, L. J. Atherton, G. A. Kyrala, J. L. Kline, R. E. Olson, D. Edgell, S. P. Regan, A. Nikroo, H. Wilkins, J. D. Kilkenny, and A. S. Moore, Phys. Plasmas **19**, 056305 (2012).
[9]J. R. Rygg, O. S. Jones, J. E. Field, M. A. Barrios, L. R. Benedetti, G. W. Collins, D. C. Eder, M. J. Edwards, J. L. Kline, J. J. Kroll, O. L. Landen, T. Ma, A. Pak, J. L. Peterson, K. Raman, R. P. J. Town, and D. K. Bradley, Phys. Rev. Lett. **112**, 195001 (2014).
[10]J. Biener, D. Ho, C. Wild, E. Woerner, M. Biener, B. El-dasher, D. Hicks, J. Eggert, P. Celliers, G. Collins, N. Teslich, Jr., B. Kozioziemski, S. Haan, and A. Hamza, Nucl. Fusion **49**, 112001 (2009).
[11]C. Dawedeit, S. O. Kucheyev, S. J. Shin, T. M. Willey, M. Bagge-Hansen, T. Braun, Y. M. Wang, B. S. El-Dasher, N. E. Teslich, M. M. Biener, J. Ye, L. Kirste, C.-C. Roehlig, M. Wolfer, E. Woerner, A. W. van Buuren, A. V. Hamza, C. Wild, and J. Biener, Diamond Relat. Mater. **40**, 75 (2013).
[12]H. F. Robey, T. R. Boehly, P. M. Celliers, J. H. Eggert, D. Hicks, R. F. Smith, R. Collins, M. W. Bowers, K. G. Krauter, P. S. Datte, D. H. Munro, J. L. Milovich, O. S. Jones, P. A. Michel, C. A. Thomas, R. E. Olson, S. Pollaine, R. P. J. Town, S. Haan, D. Callahan, D. Clark, J. Edwards, J. L. Kline, S. Dixit, M. B. Schneider, E. L. Dewald, K. Widmann, J. D. Moody, T. Doppner, H. B. Radousky, A. Throop, D. Kalantar, P. DiNicola, A. Nikroo, J. J. Kroll, A. V. Hamza, J. B. Horner, S. D. Bhandarkar, E. Dzenitis, E. Alger, E. Giraldez, C. Castro, K. Moreno, C. Haynam, K. N. LaFortune, C. Widmayer, M. Shaw, K. Jancaitis, T. Parham, D. M. Holunga, C. F. Walters, B. Haid, E. R. Mapoles, J. Sater, C. R. Gibson, T. Malsbury, J. Fair, D. Trummer, K. R. Coffee, B. Burr, L. V. Berzins, C. Choate, S. J. Brereton, S. Azevedo, H. Chandrasekaran, D. C. Eder, N. D. Masters, A. C. Fisher, P. A. Sterne, B. K. Young, O. L. Landen, B. M. Van Wonterghem, B. J. MacGowan, J. Atherton, J. D. Lindl, D. D. Meyerhofer, and E. Moses, Phys. Plasmas **19**, 042706 (2012).

[13]G. A. Kyrala, S. Dixit, S. Glenzer, D. Kalantar, D. Bradley, N. Izumi, N. Meezan, O. L. Landen, D. Callahan, S. V. Weber, J. P. Holder, S. Glenn, M. J. Edwards, P. Bell, J. Kimbrough, J. Koch, R. Prasad, L. Suter, J. L. Kline, and J. Kilkenny, Rev. Sci. Instrum. **81**, 10E316 (2010).
[14]N. B. Meezan, A. J. MacKinnon, D. G. Hicks, E. L. Dewald, R. Tommasini, S. Le Pape, T. Döppner, T. Ma, D. R. Farley, D. H. Kalantar, P. Di Nicola, D. A. Callahan, H. F. Robey, C. A. Thomas, S. T. Prisbrey, O. S. Jones, J. L. Milovich, D. S. Clark, D. C. Eder, M. B. Schneider, K. Widmann, J. A. Koch, J. D. Salmonson, Y. P. Opachich, L. R. Benedetti, S. F. Khan, A. G. MacPhee, S. M. Glenn, D. K. Bradley, E. G. Dzenitis, B. R. Nathan, J. J. Kroll, A. V. Hamza, S. N. Dixit, L. J. Atherton, O. L. Landen, S. H. Glenzer, W. W. Hsing, L. J. Suter, M. J. Edwards, B. J. MacGowan, E. I. Moses, R. E. Olson, J. L. Kline, G. A. Kyrala, A. S. Moore, J. D. Kilkenny, A. Nikroo, K. Moreno, and D. E. Hoover, Phys. Plasmas **20**, 056311 (2013).
[15]M. J. Edwards, J. D. Lindl, B. K. Spears, S. V. Weber, L. J. Atherton, D. L. Bleuel, D. K. Bradley, D. A. Callahan, C. J. Cerjan, D. Clark, G. W. Collins, J. E. Fair, R. J. Fortner, S. H. Glenzer, S. W. Haan, B. A. Hammel, A. V. Hamza, S. P. Hatchett, N. Izumi, B. Jacoby, O. S. Jones, J. A. Koch, B. J. Kozioziemski, O. L. Landen, R. Lerche, B. J. MacGowan, A. J. MacKinnon, E. R. Mapoles, M. M. Marinak, M. Moran, E. I. Moses, D. H. Munro, D. H. Schneider, S. M. Sepke, D. A. Shaughnessy, P. T. Springer, R. Tommasini, L. Bernstein, W. Stoeffl, R. Betti, T. R. Boehly, T. C. Sangster, V. Y. Glebov, P. W. McKenty, S. P. Regan, D. H. Edgell, J. P. Knauer, C. Stoeckl, D. R. Harding, S. Batha, G. Grim, H. W. Herrmann, G. Kyrala, M. Wilke, D. C. Wilson, J. Frenje, R. Petrasso, K. Moreno, H. Huang, K. C. Chen, E. Giraldez, J. D. Kilkenny, M. Mauldin, N. Hein, M. Hoppe, A. Nikroo, and R. J. Leeper, Phys. Plasmas **18**, 051003 (2011).
[16]M. Rosen, H. Scott, D. Hinkel, E. Williams, D. Callahan, R. Town, L. Divol, P. Michel, W. Kruer, L. Suter, R. London, J. Harte, and G. Zimmerman, High Energy Density Phys. **7**, 180 (2011).
[17]O. S. Jones, C. J. Cerjan, M. M. Marinak, J. L. Milovich, H. F. Robey, P. T. Springer, L. R. Benedetti, D. L. Bleuel, E. J. Bond, D. K. Bradley, D. A. Callahan, J. A. Caggiano, P. M. Celliers, D. S. Clark, S. M. Dixit, T. Döppner, R. J. Dylla-Spears, E. G. Dzentitis, D. R. Farley, S. M. Glenn, S. H. Glenzer, S. W. Haan, B. J. Haid, C. A. Haynam, D. G. Hicks, B. J. Kozioziemski, K. N. LaFortune, O. L. Landen, E. R. Mapoles, A. J. MacKinnon, J. M. McNaney, N. B. Meezan, P. A. Michel, J. D. Moody, M. J. Moran, D. H. Munro, M. V. Patel, T. G. Parham, J. D. Sater, S. M. Sepke, B. K. Spears, R. P. J. Town, S. V. Weber, K. Widmann, C. C. Widmayer, E. A. Williams, L. J. Atherton, M. J. Edwards, J. D. Lindl, B. J. MacGowan, L. J. Suter, R. E. Olson, H. W. Herrmann, J. L. Kline, G. A. Kyrala, D. C. Wilson, J. Frenje, T. R. Boehly, V. Glebov, J. P. Knauer, A. Nikroo, H. Wilkens, and J. D. Kilkenny, Phys. Plasmas **19**, 056315 (2012).
[18]L. F. Berzak Hopkins, S. Le Pape, L. Divol, N. B. Meezan, A. J. MacKinnon, D. D. Ho, M. Hohenberger, O. S. Jones, J. L. Milovich, A. Pak, J. E. Ralph, J. S. Ross, and G. A. Kyrala, "First high-convergence cryogenic implosion in a near-vacuum hohlraum," Phys. Rev. Lett. **114**, 175001 (2015).
[19]R. E. Olson, L. J. Suter, J. L. Kline, D. A. Callahan, M. D. Rosen, S. N. Dixit, O. L. Landen, N. B. Meezan, J. D. Moody, C. A. Thomas, A. Warrick, K. Widmann, E. A. Williams, and S. H. Glenzer, Phys. Plasmas **19**, 053301 (2012).
[20]L. F. Berzak Hopkins, S. Le Pape, L. Divol, N. B. Meezan, A. J. MacKinnon, D. D. Ho, O. S. Jones, S. Khan, J. L. Milovich, J. S. Ross, P. Amendt, D. Casey, A. Pak, J. L. Peterson, J. Ralph, and J. R. Rygg, "Near-vacuum hohlraums for driving fusion implosions with high-density carbon ablators," Phys. Plasmas **22**, 056318 (2015).
[21]D. E. Hinkel, M. D. Rosen, E. A. Williams, A. B. Langdon, C. H. Still, D. A. Callahan, J. D. Moody, P. A. Michel, R. P. J. Town, R. A. London, and S. H. Langer, Phys. Plasmas (1994-present) **18**, 056312 (2011).
[22]R. P. J. Town, M. D. Rosen, P. A. Michel, L. Divol, J. D. Moody, G. A. Kyrala, M. B. Schneider, J. L. Kline, C. A. Thomas, J. L. Milovich, D. A. Callahan, N. B. Meezan, D. E. Hinkel, E. A. Williams, R. L. Berger, M. J. Edwards, L. J. Suter, S. W. Haan, J. D. Lindl, E. L. Dewald, S. Dixit, S. H. Glenzer, O. L. Landen, E. I. Moses, H. A. Scott, J. A. Harte, and G. B. Zimmerman, Phys. Plasmas **18**, 056302 (2011).
[23]P. Michel, L. Divol, E. Williams, S. Weber, C. Thomas, D. Callahan, S. Haan, J. Salmonson, S. Dixit, D. Hinkel, M. Edwards, B. MacGowan, J. Lindl, S. Glenzer, and L. Suter, Phys. Rev. Lett. **102**, 025004 (2009).
[24]P. W. Rambo and J. Denavit, Phys. Plasmas **1**, 4050 (1994).
[25]D. E. Hinkel, D. A. Callahan, A. B. Langdon, S. H. Langer, C. H. Still, and E. A. Williams, Phys. Plasmas **15**, 056314 (2008).
[26]J. E. Field, J. R. Rygg, M. A. Barrios, L. R. Benedetti, T. Döppner, N. Izumi, O. Jones, S. F. Khan, T. Ma, S. R. Nagel, A. Pak, R. Tommasini, D. K. Bradley, and R. P. J. Town, Rev. Sci. Instrum. **85**, 11E503 (2014).
[27]M. Gatu Johnson, J. A. Frenje, D. T. Casey, C. K. Li, F. H. Séguin, R. Petrasso, R. Ashabranner, R. M. Bionta, D. L. Bleuel, E. J. Bond, J. A. Caggiano, A. Carpenter, C. J. Cerjan, T. J. Clancy, T. Doeppner, M. J. Eckart, M. J. Edwards, S. Friedrich, S. H. Glenzer, S. W. Haan, E. P. Hartouni, R. Hatarik, S. P. Hatchett, O. S. Jones, G. Kyrala, S. Le Pape, R. A. Lerche, O. L. Landen, T. Ma, A. J. MacKinnon, M. A. McKernan, M. J. Moran, E. Moses, D. H. Munro, J. McNaney, H. S. Park, J. Ralph, B. Remington, J. R. Rygg, S. M. Sepke, V. Smalyuk, B. Spears, P. T. Springer, C. B. Yeamans, M. Farrell, D. Jasion, J. D. Kilkenny, A. Nikroo, R. Paguio, J. P. Knauer, V. Yu Glebov, T. C. Sangster, R. Betti, C. Stoeckl, J. Magoon, M. J. Shoup, G. P. Grim, J. Kline, G. L. Morgan, T. J. Murphy, R. J. Leeper, C. L. Ruiz, G. W. Cooper, and A. J. Nelson, Rev. Sci. Instrum. **83**, 10D308 (2012).
[28]S. F. Khan, P. M. Bell, D. K. Bradley, S. R. Burns, J. R. Celeste, L. S. Dauffy, M. J. Eckart, M. A. Gerhard, C. Hagmann, D. I. Headley, J. P. Holder, N. Izumi, M. C. Jones, J. W. Kellogg, H. Y. Khater, J. R. Kimbrough, A. G. Macphee, Y. P. Opachich, N. E. Palmer, R. B. Petre, J. L. Porter, R. T. Shelton, T. L. Thomas, and J. B. Worden, Proc. SPIE **8505**, 850505 (2012).
[29]A. Pak, L. Divol, G. Gregori, S. Weber, J. Atherton, R. Bennedetti, D. K. Bradley, D. Callahan, D. T. Casey, E. Dewald, T. Döppner, M. J. Edwards, J. A. Frenje, S. Glenn, G. P. Grim, D. Hicks, W. W. Hsing, N. Izumi, O. S. Jones, M. G. Johnson, S. F. Khan, J. D. Kilkenny, J. L. Kline, G. A. Kyrala, J. Lindl, O. L. Landen, S. Le Pape, T. Ma, A. MacPhee, B. J. MacGowan, A. J. MacKinnon, L. Masse, N. B. Meezan, J. D. Moody, R. E. Olson, J. E. Ralph, H. F. Robey, H.-S. Park, B. A. Remington, J. S. Ross, R. Tommasini, R. P. J. Town, V. Smalyuk, S. H. Glenzer, and E. I. Moses, Phys. Plasmas **20**, 056315 (2013).
[30]D. Salzmann, *Atomic Physics in Hot Plasmas*, International Series of Monographs on Physics (Oxford University Press, USA, 1998).
[31]T. Ma, P. K. Patel, N. Izumi, P. T. Springer, M. H. Key, L. J. Atherton, L. R. Benedetti, D. K. Bradley, D. A. Callahan, P. M. Celliers, C. J. Cerjan, D. S. Clark, E. L. Dewald, S. N. Dixit, T. Döppner, D. H. Edgell, R. Epstein, S. Glenn, G. Grim, S. W. Haan, B. A. Hammel, D. Hicks, W. W. Hsing, O. S. Jones, S. F. Khan, J. D. Kilkenny, J. L. Kline, G. A. Kyrala, O. L. Landen, S. Le Pape, B. J. MacGowan, A. J. Mackinnon, A. G. MacPhee, N. B. Meezan, J. D. Moody, A. Pak, T. Parham, H.-S. Park, J. E. Ralph, S. P. Regan, B. A. Remington, H. F. Robey, J. S. Ross, B. K. Spears, V. Smalyuk, L. J. Suter, R. Tommasini, R. P. Town, S. V. Weber, J. D. Lindl, M. J. Edwards, S. H. Glenzer, and E. I. Moses, Phys. Rev. Lett. **111**, 085004 (2013).